Single-molecule imaging of cholesterol-dependent cytolysin assembly

Michael J Senior[1], Carina Monico[1,2], Eve E Weatherill[2], Robert J Gilbert[3], Alejandro P Heuck[4], Mark I Wallace[2]

[1] Chemistry Research Laboratory, Department of Chemistry, University of Oxford, Oxford OX1 3TA, United Kingdom.

[2] Department of Chemistry, King's College London, London SE1 1DB, United Kingdom,

[3] Division of Structural Biology, Wellcome Centre for Human Genetics, University of Oxford, Roosevelt Drive, Oxford OX3 7BN, United Kingdom,

[4] Departments of Biochemistry and Molecular Biology, University of Massachusetts, Amherst, MA, USA

E-mail: `mark.wallace@kcl.ac.uk`

Compiled 26 May 2021

Abstract. We exploit single-molecule tracking and optical single channel recording in droplet interface bilayers to resolve the assembly pathway of the Cholesterol-Dependent Cytolysin, Perfringolysin O. This enables quantification of the stoichiometry of PFO complexes during assembly with millisecond temporal resolution and 20 nanometre spatial precision. Our results support a model of overall stepwise irreversible assembly, dominated by monomer addition, but with infrequent assembly from larger partial complexes. Furthermore, our results suggest a dominant proportion of inserted, but non-conductive intermediates in assembly.

1. Introduction

The Membrane Attack Complex Perforin / Cholesterol Dependent Cytolysin (MACPF/CDC) protein superfamily form large multimeric β-barrel pores in the membranes of target cells. For example, Perfringolysin O (PFO) assembles 30-50 monomers to form a single giant pore with a diameter of over 25 nm ([1, 2, 3, 4]).

MACPF proteins are a key component of the human immune system, using pore formation to lyse the cells of invading bacteria ([5]). CDCs perform the analogous role in bacteria, and are virulence factors in a wide range of pervasive diseases including pneumococcal meningitis and listeriosis ([6, 7]). Beyond just pore formation, MACPF/CDCs are also thought to play important roles ([8]) in processes as varied as histone modification ([9]), lipid raft aggregation ([10]), and the control of embryonic development ([11]).

MACPF/CDCs are defined by a common β-barrel structural motif ([12]), suggesting not only interesting evolutionary links between the two families ([13]) but also strong similarities in the mechanism of pore formation. Thus understanding the assembly pathway for one branch of proteins has broad implications across the superfamily.

The model for MACPF/CDC pore formation is one where monomers first bind to a cell membrane, then oligomerize into arc and ring-shaped (prepore) complexes, before finally folding cooperatively to insert a β-barrel that punctures the membrane ([14, 15, 16, 17, 12, 18, 19, 20, 21]). Evidence for this model of pore formation has been primarily provided by a range of protein structures and ensemble kinetic experiments ([22, 23, 24, 25, 26, 3, 27, 28]). Beyond this well-established general scheme, much is still unclear regarding the kinetics of pore insertion.

To shed further light on the mechanism of pore assembly, a combination of high temporal and spatial resolution is required; where both pore dynamics and the nature of the forming complex can be resolved. Hoogenboom and co-workers recently used high-speed AFM to study assembly of suilysin ([29, 20]), perforin ([30]), and most recently membrane attack complex ([31]), while others have also used it with listeriolysin ([32, 19]) and perforin-2 ([27]). Here, we seek to improve on this temporal resolution by imaging the assembly of individual PFO pores using single-molecule fluorescence microscopy in Droplet Interface Bilayer (DIB) model membranes ([33, 34]). This enables quantification of the stoichiometry of PFO complexes during assembly with millisecond temporal and diffraction-limited (223 nm) spatial resolution with super-resolved spatial precision (20 nm). Our results support a model of overall stepwise irreversible assembly, dominated by monomer addition, but with infrequent assembly from larger partial complexes. Furthermore, our results suggest a dominant proportion of inserted, but non-conductive intermediates in assembly.

2. Results

2.1. Imaging the assembly of individual PFO complexes.

We used single-molecule imaging with our previously developed DIB platform ([34]) to examine the assembly of individual monomers into large complexes and conductive pores. DIBs were created by the contact of two monolayers formed at oil-water interfaces on a sub-micron thick agarose film, allowing the bilayer to be imaged with single-molecule total internal reflection fluorescence (TIRF) microscopy. DIBs also enable control of the membrane potential, with GΩ electrical seals compatible with single-channel recording ([35]).

Bilayers were formed with a mixture of 1,2-diphytanoyl-*sn*-glycero-3-phosphocholine (DPhPC) and Cholesterol. After bilayer formation, PFO was injected into the aqueous droplet to a final concentration of 37 nM using a piezo-controlled nanopipette (1a, see methods for further details). A mixture of PFO labelled with Alexa-488 (PFO-a488) and unlabelled PFO (1:5.5 molar ratio) was used to optimise signal amplitude and minimise

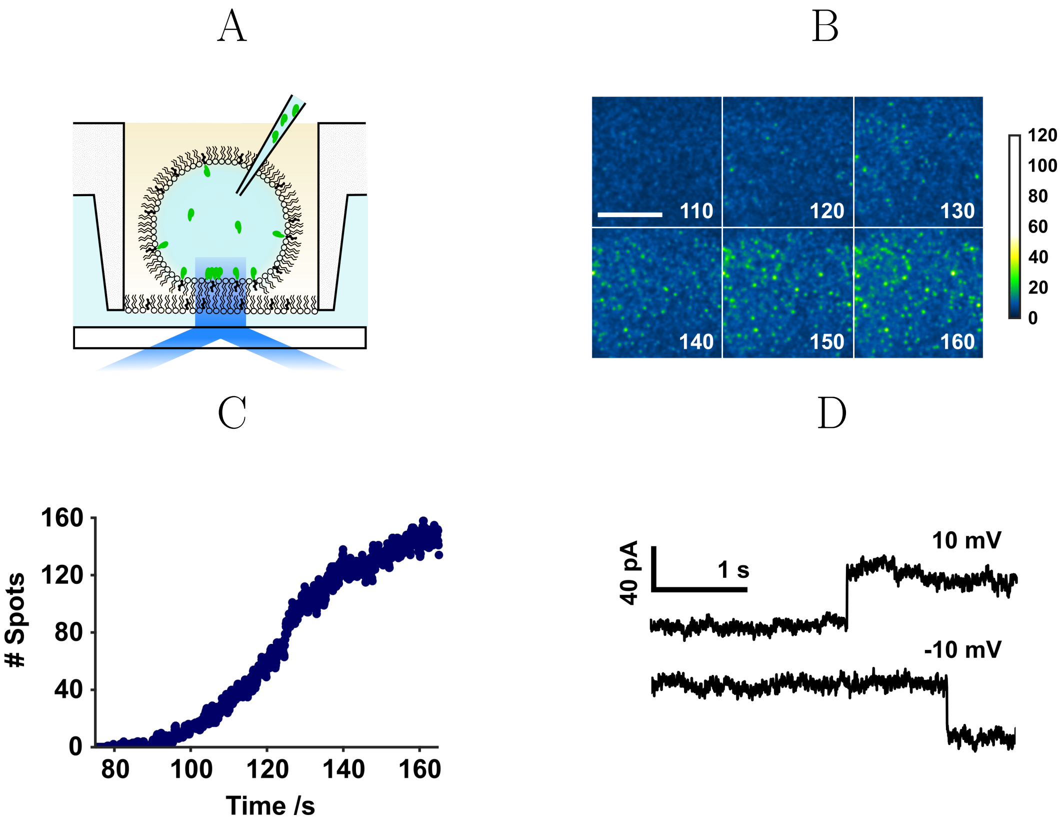

Figure 1: **Experimental design.** (A) Schematic of PFO (green) injection into a DIB contained in a microfabricated plastic well. The bilayer rests on a submicron thick agarose layer to enable TIRF imaging of the labelled protein on the bilayer. (B) Over time, PFO assembly was observed. PFO complexes, containing many labelled monomers appear as bright spots (green), with higher intensity than the monomer (blue). Images are blue-green false-coloured to aid discrimination, with a scale normalized to the intensity of a monomer. White numbering denotes seconds following protein injection. Image acquisition rate 16.67 Hz. Scale bar 25 µm. (C) Total number of spots detected in the video represented in B. (D) Electrodes placed in the hydrogel and the droplet permit measurement of current across the bilayer. Rarely, stepwise 4 nS changes in conductance were observed, consistent with insertion of single PFO pores into the bilayer.

fluorescence self-quenching ([36]).

Protein monomers were observed to bind to the bilayer and diffuse freely (1b). Analogous to our previous work on *Staphylococcus aureus* α-hemolysin ([37]) spots with an intensity greater than that of a single fluorophore appeared over time (1b, 1c), consistent with the formation of oligomeric PFO complexes. Trackmate ([38]) a tracking algorithm implemented as a Fiji ([39]) plugin was applied to detect spots brighter than a single monomer (1C). Both the number and intensity of individual spots increased over time, before reaching a plateau (1c, 2C, ***Movie S1***). Complex assembly was cholesterol dependent: binding was not observed in cholesterol-free bilayers.

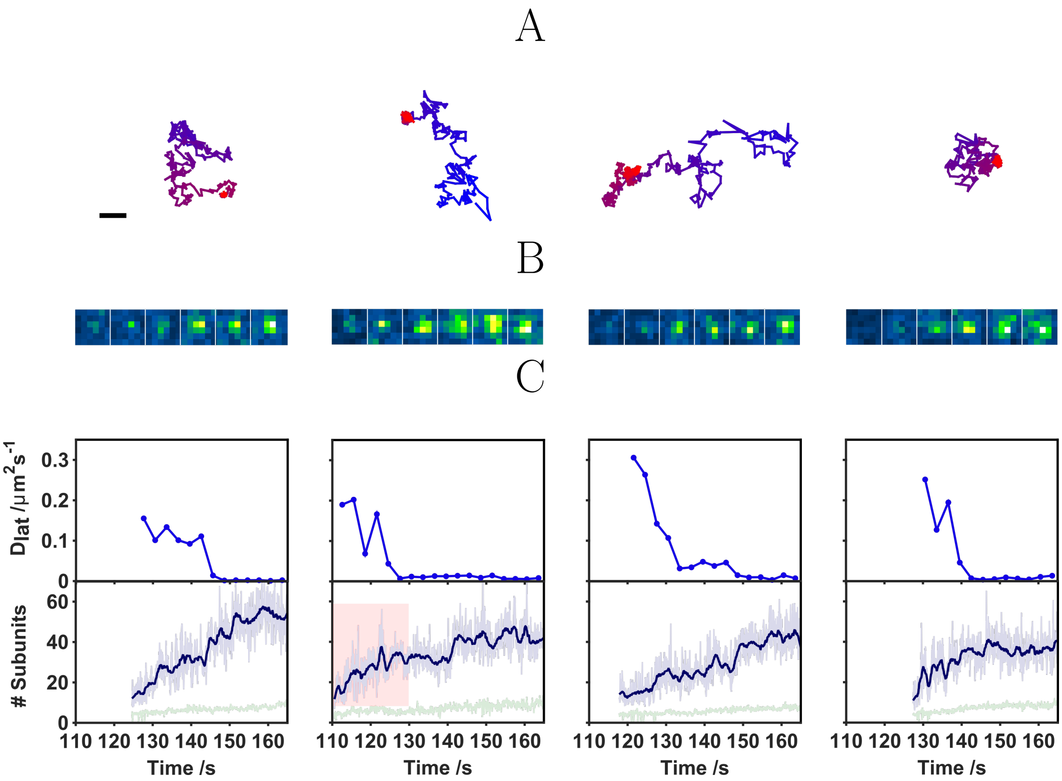

Figure 2: **Assembly of individual complexes.** Each column is a representative assembly event from our dataset. (A) Track coordinates of a complex over time (blue to red). Scale bar 1 µm. (B) Raw image intensity for a 6 × 6 pixel region of interest (ROI) coinciding with the appearance of the complex. Images are at 20 s intervals. (C) Time-dependent diffusion coefficient of the complex, calculated from the coordinates displayed in (A) (averaging over 3 s intervals); stoichiometry of the complex as a function of time. Raw values (light blue) and a 1.26 s running average (dark blue) is shown. The local background signal is also plotted (green). The red highlighted section corresponds to data used in (***Figure S1***).

2.2. Single pore conductance.

By inserting Ag/AgCl microelectrodes into the droplet and agarose substrate, the ionic flux across the bilayer was measured ([34]). Individual PFO insertion events were detected as rare stepwise changes in conductance of approximately 4 nS (1d), corresponding to previously reported values for PFO ([40]) and other CDCs ([41, 42, 43]).

2.3. Pore stoichiometry.

The stoichiometries and time-dependent diffusion coefficients for complexes were then determined. 2 shows the assembly of four representative complexes from the dataset corresponding to 1b. Each column in 2 represents an individual complex. The position (2a), raw intensity data (2b), time-dependent diffusion coefficient, and stoichiometry (2c) are shown. The time-dependent diffusion coefficients were calculated from the mean squared displacement over 3 second intervals. Notably, complexes often show a marked decrease in diffusion coefficient during assembly, present as a rapid drop in diffusion (2c). PFO stoichiometry was determined from the fraction of labelled PFO (1 A488 label per 6.5 PFO monomers) and normalisation of the time-dependent change in complex intensity to that measured for isolated single PFO-a488 monomers (***Figures S2&3***). The stoichiometry increases essentially monotonically within an individual complex (2c). Higher intensity complexes are correlated with lower protein mobility (3e), with the decrease in the diffusion constant often coinciding with a plateau in stoichiometry (2c).

2.4. Kinetics of assembly.

A key advantage of tracking individual complexes is the ability to examine the protein population without the need for extrinsic synchronisation of the ensemble (for example via chemical modification such as disulphide locking ([25])). To analyse the collective behaviour, we examined all tracks that start with an initial stoichiometry below 20 to ensure effective averaging of the kinetics associated with early assembly. Trajectories were analysed by aligning the times at which each complex was first detected. 3a depicts individual trajectories (light blue) and their median (dark blue). Overall, the assembly is described by an initial period of rapid growth, before a slower extension of the complex, best fit by a double-exponential (3a, red line). The corresponding pseudo-first order rate constants for assembly are $k_1 =$ 2.2 s^{-1} and $k_2 =$ 0.05 s^{-1}. Of the two, k_2 dominates (78%) and broadly matches the overall timescale for the number of complexes appearing over time (1c). The rate of assembly taken from this curve represents the number of successful collisions with monomers for a single complex per second. At the inflexion point when complexes are appearing most rapidly (125 seconds after injection in 1c), the density of complexes is 0.03 µm^{-2}. Thus, an estimate of the overall maximum rate for the assembly (rate of successful collisions between monomers and complexes) at this surface density is 0.0015 µm^{-2} s^{-1}.

The rate of collision (ν) between monomers and nascent complexes can be estimated by employing a simple 2D diffusion model ([44]): Making the assumption that complexes can be approximated as static sinks relative to monomers, and that collisions occur below a fixed encounter radius,

$$\nu = \frac{2\pi D_{\mathrm{m}}\rho_{\mathrm{m}}\rho_{\mathrm{c}}}{\ln b/R - \gamma + \ln\sqrt{2}}. \tag{1}$$

Here $\rho_{\mathrm{c}} = 0.03$ µm^{-2} is the surface density of complexes determined from the number of complexes per area at the inflexion point in 1c; $\rho_{\mathrm{m}} = 14$ µm^{-2} is the surface density of single free monomers; estimated by dividing the overall intensity per unit area of the bilayer at the inflexion point by the intensity of a single monomer (***Figure S2***). The diffusion coefficient for single monomers ($D_{\mathrm{m}} = 1.5$ µm^2 s^{-1}) was determined from the mean square displacement vs. time for labelled monomers diffusing on the bilayer. The encounter radius within which a collision is deemed to have occurred, R, was set at 2.75 nm - approximating the radius of a PFO monomer ([22]). $\gamma = 0.577$, the Euler-Mascheroni constant and $b = \sqrt{(\pi\rho_{\mathrm{c}})^{-1}}$. The rate for monomer-complex collisions

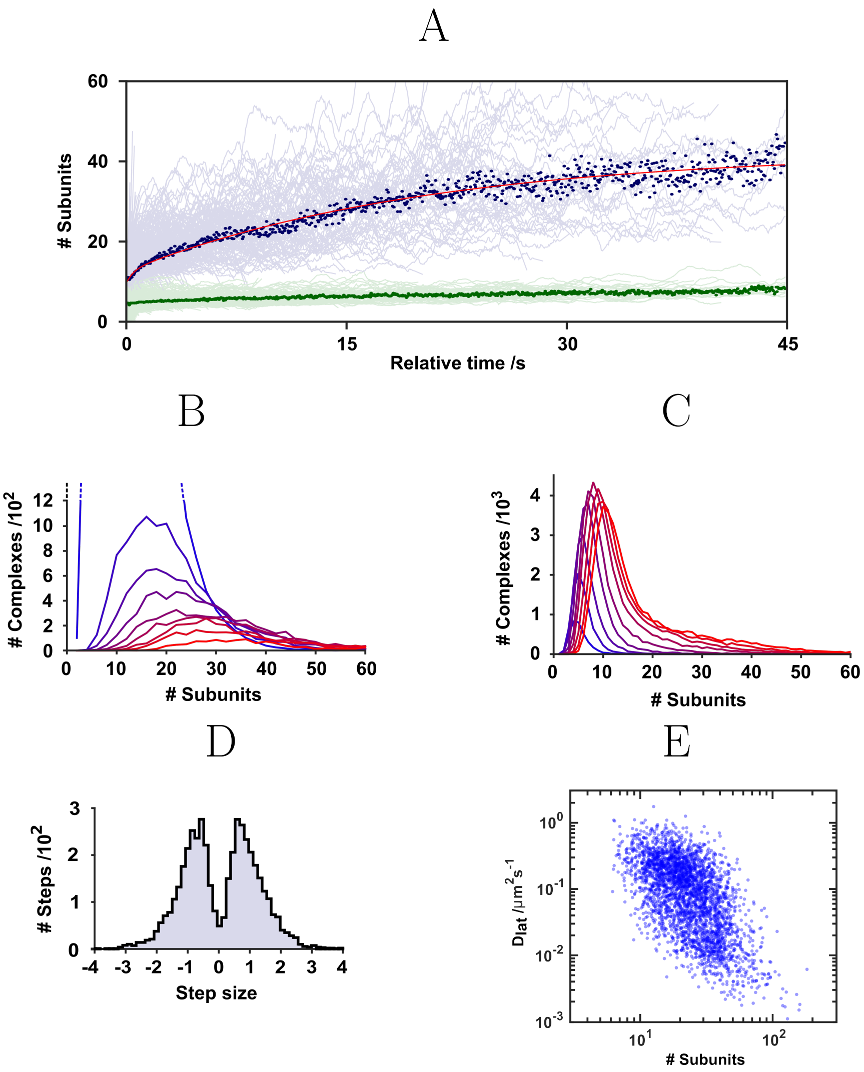

Figure 3: **Overall kinetics of assembly.** (A) Assembly events were temporally-aligned and plotted (light blue lines). A threshold on trajectories was applied to select those with an initial stoichiometry of 20 subunits or fewer to ensure temporal alignment captured early assembly. The median of these trajectories is superposed (dark blue dots), representing the average rate of assembly of a single complex, best fit to a double exponential (red line). The equivalent background signal from these trajectories is also shown (green). (B) Tracking parameters were then adjusted to include monomers (as opposed to just complexes as per 3a), tracks were aligned as in (A), and stoichiometry histograms corresponding to 5 second intervals are plotted and color-coded (blue to red). The histogram peak position shifts over time in the assembly process, as a large number of small oligomers (blue) are converted to smaller numbers of larger complexes (red). (C) Equivalent histograms as (B), but without alignment of the tracks shows the overall evolution of PFO during assembly. Histograms show the change in overall PFO complex size since the injection of protein into the droplet. Each histogram corresponds to a 10 second interval (color-coded blue to red). (D) A histogram of step-sizes, normalised to the intensity of a single fluorophore, indicates the most common event is a single monomer arriving at or leaving the vicinity of the complex. (E) Trajectories for a representative 500 tracks were segmented at 1.2 second intervals and the diffusion coefficient determined for each segment. The diffusion coefficient was then plotted against mean stoichiometry for each corresponding segment. An approximately power law relation between D_{lat} and stoichometry was observed ($D_{\mathrm{lat}} \propto S^{-3.8}$).

determined from this analysis is $k = 0.58\ \mu\text{m}^{-2}\ \text{s}^{-1}$.

Comparing the rate for monomer-complex collisions to the overall rate of complex assembly ($0.0015\ \mu\text{m}^{-2}\ \text{s}^{-1}$), 1 in 390 collisions between monomers and nascent complexes are successful and result in growth. Collisions are thus likely to lead to assembly. This is very different to our previous work on the heptameric β-barrel toxin α-hemolysin ([37]) where only 1 in 10^7 collisions were successful. Whereas α-hemolysin requires reversible assembly, the high assembly probability for PFO provides evidence for a different, irreversible, assembly mechanism. An irreversible stepwise monomer-addition mechanism for PFO is arguably expected based on the large number of monomers forming MACPF/CDC pores. Irreversible assembly is supported by other data ([20, 45]).

3b depicts the variation in the distribution of PFO stoichiometries with time, synchronised to the start of assembly of each complex. Here, tracking parameters were optimised to detect monomers as well as protein complexes. As expected, a shift from smaller to larger complexes with time is observed with a broad distribution of final complex sizes (30 – 40 subunits). The number of low-stoichiometry complexes and monomers in the first 5 seconds is high (19200) relative to the later peaks, due to the excess of monomers on the bilayer at early stages of assembly. We also examined the events in 3b not relative to assembly, but in real time, sampled every 10 seconds after injection of the protein in the bilayer (3c). The overall peak area increases over time as more monomers bind to the bilayer. In addition, over time the tail of this distribution elongates as the mean stoichometry transitions towards higher, assembled, complexes. However, there are always more monomers on the bilayer than complexes, and the low-stoichiometry peak dominates.

We can also examine more closely the apparent time-dependent change in stoichiometry within an individual complex (3c). For these data, we observed significant fluctuations in intensity whilst showing the overall upward trend. These fluctuations are accurately captured by a step-finding algorithm ([46]) (***Figure S1***). A histogram of the step-sizes (3d) exhibits two peaks with a median step-size of ±1 monomer intensity units. This indicates that the majority of steps found by the algorithm correspond to a single labelled monomer in the vicinity of the complex. It also corroborates our estimate of the single-fluorophore intensity (***Figure S2***). Unfortunately given the frequency of successful collisions relative to the maximum stoichiometry of a final complex, it is unlikely that these steps correspond to the dynamic addition or removal of monomers from a nascent complex; it is more likely that these steps correspond in general to the diffusion of monomers nearby the forming complex. As expected, we also observe a weak dependence of the diffusion coefficient of a complex on its size (3e, [47]).

2.5. Complex plasticity.

After characterising the overall trend of monomer addition and growth, we examined more closely those events that showed evidence of interaction between larger nascent

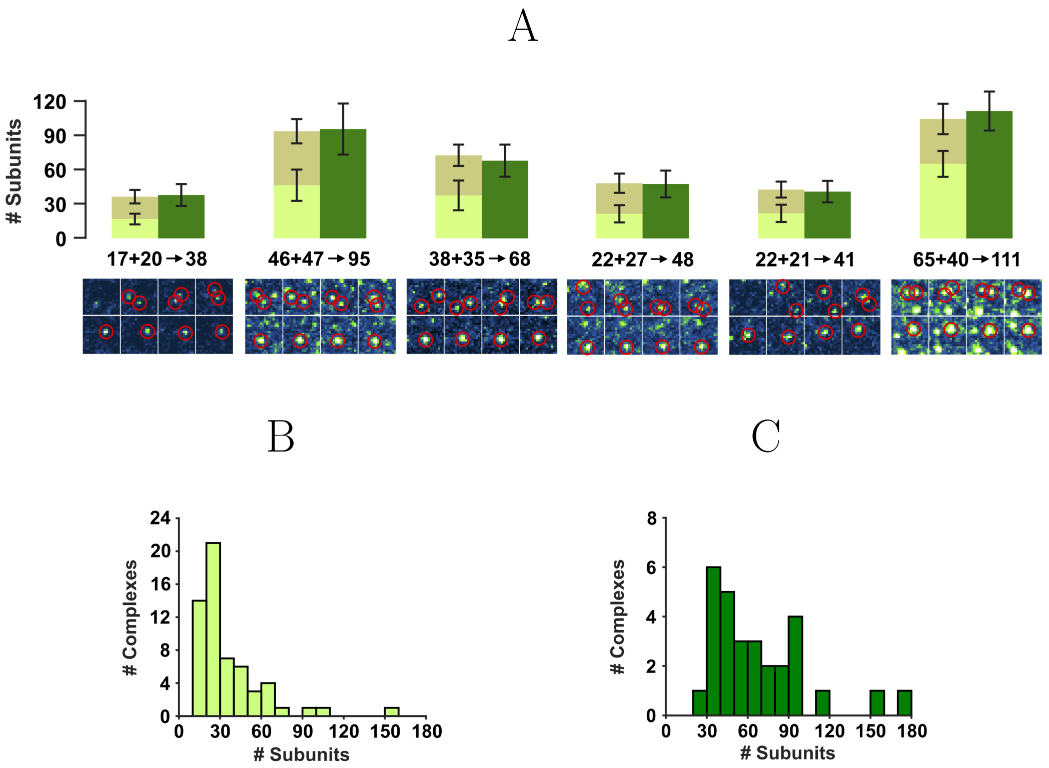

Figure 4: **PFO plasticity.** (A) Partial complexes we observed to join to form larger complexes; events were analysed for their stoichiometries, by averaging 50 frames before (light green/brown) and after (dark green) the merging event. The position of each complex is highlighted in the image sequence below, the frames displayed being taken at -10, -5, -2.5, -1.25, 0, 1.25, 2.5 and 5 seconds relative to the event. (B) Histogram of complex stoichiometries before merging (median = 26). (C) Histogram of complex stoichiometries after merging (median = 58).

complexes. During assembly, diffusing multi-subunit complexes were observed to encounter each other and combine. As our spatial resolution is diffraction-limited, to correctly define a merging event those complexes must not only reside within the same spot, but also persist for longer than the expected diffusion time for a single complex. For comparison, we observed 30 merging events in more than 500 tracked complexes.

4 and ***Movie S2*** present examples of plasticity events: the montages in 4a highlight the merging events as they appear for each event (at -10, -5, -2.5, -1.25, 0, +1.25, +2.5, +5 seconds relative to the event). The stoichiometry of the resulting complex closely matches the combined stoichiometry of the initial complexes. This analysis was performed for 30 complexes: 4b and 4c are the corresponding histograms of PFO stoichiometry for before and after each merging event. The median complex stoichiometries before and after merging are 26 and 58 respectively. We also observe changes in diffusivity associated with plasticity. Events were observed in which: mobile complexes joins a significantly less mobile complex; two diffusing complexes merge and exhibit a concomitant decrease in mobility; two mobile complexes merge and subsequently diffuse away along the same trajectory.

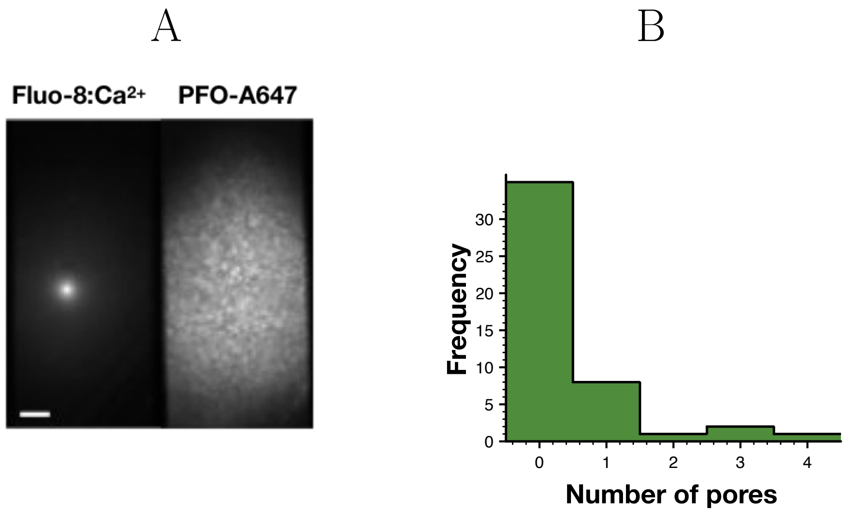

Figure 5: **Dual-color imaging of pore formation.** (A) Pores are detected optically in the left channel from fluorescence emitted by Fluo-8, a calcium sensitive dye as it flows through the pore. The right channel reports on fluorescence from PFO labelled with Alexa-647. Pores form rarely relative to the large number of assembled complexes. Scale bar 2µm. (B) Distribution of PFO pore events per bilayer as determined by Fluo-8 imaging of calcium flux.

2.6. Pore formation.

After assembly, PFO forms pores in the membrane. To follow this process we combined simultaneous optical recording of ionic flux ([35]) with single-molecule fluorescence imaging to enable comparison between pore formation and assembly. The presence of pores in the membrane was detected by imaging Fluo-8, a calcium sensitive dye, while the extent of oligomerization of monomers into complexes was measured by imaging PFO labelled with Alexa-647 (5a). Alexa-647 was chosen to enable simultaneous imaging of both calcium flux and oligomerisation. As with our previous work on other pore-forming proteins ([37, 48]), the ionic flux-induced fluorescence intensity of a single pore varies linearly with the voltage applied across the bilayer (***Figure S4***). Surprisingly, relative to the number of assembled complexes on the bilayer, we only observed rare conductive pores (5b). Pores were only detected under conditions where individual PFO complexes could not be resolved by single-molecule fluorescence due to high concentration (5a, right channel). Nonetheless, simultaneous electrical and optical recordings show that once formed, PFO pores were extremely stable (often lasting several hours) with differing but stable conductance (1d, 5a, ***Figure S4***).

3. Discussion

Our measurements provide a broad overview of PFO assembly from early- to late-stages of pore formation (1 and 2). Overall, these results are in agreement with the accepted model for CDC pore assembly, with irreversible monomer addition followed by pore insertion. However our high temporal resolution coupled with single-molecule sensitivity enables further insight.

Overall, we observe bi-component assembly kinetics (3) with rapid oligomerization in early stages followed by a period of slower extension of the oligomer. These kinetics are reminiscent of the two-step mechanism reported for streptolysin-O, where membrane-bound dimerisation is followed by sequential oligomerization ([49]), and for the initial conformation change reported for PFO ([50]) and other CDCs ([21, 51]).

Although there is a broad distribution of individual assembly rates, in essence all complexes follow the same assembly pathway (3a), with little evidence of different modes of assembly or trapped intermediates. The distribution of PFO stoichiometry over time (3b) is characterised by a broad distribution in the number of subunits throughout all stages of PFO assembly, consistent with the reported variable pore sizes typical of CDC oligomers ([18, 26, 20, 52]). Additionally, Tweten and colleagues used NBD attached to a cysteine-substituted derivative of PFO to suggest that oligomerization is favoured over initiation of new complexes ([40]), a model supported by our data.

Our results support a model of PFO assembly consistent with an irreversible stepwise addition of monomers to assembling complexes. This is mainly evidenced by the continuous growth to larger complexes (2, 3a, 3b, 3c) and by the number of successful collisions. Only 1 in 340 collisions lead to successful oligomerization, surprisingly many compared to reversible assembly of other oligomeric proteins ([37]). It's possible that this difference may be accounted for by the cooperative nature of α-HL assembly, whereas the scale of CDC oligomers may instead require some kind of switching mechanism to retain monomers once they join ([51]). This supports an irreversible model of CDC assembly as also evidenced by cryoEM and AFM ([45, 20]).

Examining the assembly of individual complexes 2 shows fluctuations in intensity are consistent with the addition of single, but not multiple, fluorescently labeled monomers. Given our labelling ratio, (1 fluorophore per 6.5 monomers), the occurrence and detection of oligomers smaller than this size would be low. Labelling only a fraction of the monomers minimises fluorophore - fluorophore interactions. Once complexes appeared they do not dissociate (***Movie S1***). This is also consistent with a model based on irreversible assembly of monomers and in agreement with previous reports ([23, 45]), where completion of existing complexes is favoured over the initiation of new complexes. Ultimately, our insight into these early kinetics is limited by the the competing requirements of sub-stoichiometric labelling and the need to discriminate between nascent complexes and the surrounding milieu of monomers.

We were able to track the assembly of individual complexes with 20 nm precision, which is the x-error in fitting of the point spread function of a spot. Closer examination of these tracks also revealed a stepwise drop in the diffusion coefficient to near static during assembly, rather than after (2). A likely cause for this change would be the transmembrane insertion of a portion of the complex which becomes stuck on the underlying agarose. This would be consistent with previous reports of transmembrane insertion of oligomers prior to full pore formation ([20, 18]). However, we were surprised that simultaneous Ca^{2+} flux imaging (5) showed that only few of these inserted complexes were able to conduct ions. Overall this would support a mechanism that incorporates transmembrane membrane insertion of one or more β-hairpins, but not formation of a conductive pore. CDC pore formation kinetics is temperature dependent ([40]), however, our efforts to repeat these experiments at higher temperature (37°C) resulted in no appreciable increase in kinetics of pore formation. Optical single-channel recording (5) and electrophysiology (1d) confirm that successful insertion is possible under our experimental conditions and lipid compositions. PFO insertion has has been shown previously in liposomes prepared with DPhPC and Cholesterol ([53]).

Fusion of incomplete arc-shaped complexes has been hypothesised as a mechanism of pore assembly ([54, 55, 56]), supported by time-lapse AFM images for listeriolysin O (5 minutes time interval, for a total of 4 consecutive images) ([32, 19]). Additionally, disassembly and reassembly of such structures was also observed in PFO1 ([42]). Our single-molecule data show real-time evidence of plasticity in PFO complexes (4), supporting a model in which the fusion of partially assembled oligomers contributes to pore formation in CDCs. Although present, these events represent a small fraction ($\approx 0.1\%$) of the overall assembly process which must be dominated by monomer or small (n¡6) oligomer addition.

In summary, this method provides a high time-resolution complement to the higher spatial resolution single-molecule information provided by AFM and EM. Overall, our ability to follow in real-time every single CDC complex without the need for chemical synchronisation of the population supports a better understanding of the CDC mechanism of assembly, including access to important, but rare, events.

4. Methods and Materials

4.1. PFO.

A single cysteine mutant of PFO (PFO[C459A, E167C]) and PFO[C459A] were expressed in *E. coli* and purified ([57]). PFO[C459A, E167C] was 1:1 labelled via maleimide coupling chemistry with Alexa-488 or Alexa-647. E167 was chosen as it is situated on the 'top' of the monomer, relative to the membrane, and so does not influence the pore assembly mechanism ([58]).

Alexa-labelled PFO was separated from free dye by gel filtration in 50 mM HEPES, 100 mM NaCl, pH 7.5 and stored with 10% glycerol at -80°C. Labelling efficiency was 100% for Alexa-488 and 68% for Alexa 647. A haemolytic assay was performed to verify the biological functionality of the protein. PFO was reconstituted at pH 6.5 ([53]) in fluorescence imaging buffer (0.5 M KCl, 10 mM MES, 0.1 mM EDTA, 1 mM Trolox and 10 mM Cysteamine) before injection into the droplet.

4.2. Droplet Interface Bilayers

(DIBs) were created by the contact of two monolayers formed at oil-water interfaces. First, a monolayer was formed around a 138 nl aqueous droplet with 8.5 mg ml^{-1} of 1,2-

diphytanoyl-*sn*-glycero-3-phosphocholine (DPhPC) in 10% silicone oil in hexadecane. Meanwhile, a second monolayer of 15.5 mg ml^{-1} 1:2 DPhPC:cholesterol in hexadecane was formed on a sub-micron thick agarose film (0.75% w/v low-melt agarose in water), spin-coated on a coverslip within a PMMA micro-machined device ([34]). 1.8% w:v of low melt agarose in the same buffer, was added around the PMMA chamber for hydration. The monolayers were incubated for 2.5 hours at RT, and then the 138 nl droplet was pipetted into the well to form a bilayer upon the contact of the two monolayers. The bilayer was then heated for 30 minutes at 37°C to allow equilibration of the asymmetric monolayers (this is longer than the half-life for cholesterol flip-flop (50 min at 25°C ([59])). Subsequently the agarose film was further rehydrated by fusing a 2.3 nl volume of buffer to it from a nanolitre piezo-injector (World Precision Instruments). Once the imaging conditions had been optimized, 4.6 nl of PFO (PFO-a488:PFO, 1:5.5) in solution was piezo-injected into the 138 nl droplet to a final total concentration of PFO in the droplet of 37 nM. Imaging was initiated not more than 30 seconds after injection of the protein.

4.3. Imaging and data analysis.

Total Internal Reflection Fluorescence imaging of the bilayer following injection of the protein solution was performed using a customized Nikon Eclipse TiE inverted microscope equipped with an APO 60× 1.45 NA oil-immersion objective. Videos were recorded on an electron-multiplying camera (Andor Ixon). Events were tracked using the TrackMate plugin for Fiji/ImageJ ([39, 38]). Once the coordinates had been extracted for each spot in the tracks, a Gaussian function was fitted to the spots at the specified coordinates in the original video, to extract the spot amplitude, background and x, y positions. This fitting and all further analysis was performed using custom software written in Matlab. Diffusion coefficients for 3 second (2) and 1.2 second (***Figure S2***) intervals were determined by fitting of the mean-squared-displacement vs time.

4.4. Electrical recordings and dual-colour imaging

138 nL droplets contained Fluo-8 20 ug mL^{-1} in 10 mM MES buffer pH 6.5, 1 M KCl, 0.14 mM EDTA, and hydration agarose (2% w:v) in 0.5 M $CaCl_2$, 0.1 mM EDTA in 10 mM MES pH 6.5. A symmetric bilayer was prepared with 16 mg ml^{-1} of DPhPC:Chol 1:2 in 20% silicone oil in hexadecane. A ground electrode was added to the agarose and the reference electrode to the droplet (***Figure S6***) connected to a CV-203BU headstage and an Axopatch 200B amplifier (Axon Instruments). The droplets and electrodes were contained in a Faraday cage. An emission image splitter (Cairn OptoSplit) was added in the camera to enable simultaneous recording of the green (Fluo-8) and FarRed (Alexa-647 PFO) channels. Initially, a mixture of 1:5.5 rPFOE167C-Alexa-647:rPFO was injected to the droplet to a final concentration of 45 nM, and equivalent assembly videos were acquired, as in the case of 1-colour imaging with PFO-Alexa-488. For experiments in 5 the PFO concentration was increased to 100 nM.

5. Acknowledgments

MJS was funded by the EPSRC Life-Science Interface Doctoral Training Centre.

6. References

[1] Olofsson A, Hebert H and Thelestam M 1993 *FEBS Letters* **319** 125–127

[2] Dang T X, Hotze E M, Rouiller I, Tweten R K and Wilson-Kubalek E M 2005 *Journal of Structural Biology* **150** 100–108

[3] Hotze E M and Tweten R K 2012 *Biochimica et Biophysica Acta (BBA) - Biomembranes* **1818** 1028–1038

[4] Johnson B B and Heuck A P 2014 *Perfringolysin O Structure and Mechanism of Pore Formation as a Paradigm for Cholesterol-Dependent Cytolysins* (Dordrecht: Springer Netherlands) pp 63–81 ISBN 978-94-017-8881-6

[5] Rosado C J, Kondos S, Bull T E, Kuiper M J, Law R H P, Buckle A M, Voskoboinik I, Bird P I, Trapani J A, Whisstock J C and Dunstone M A 2008 *Cellular Microbiology* **10** 1765

[6] Reiß A, Braun J S, Jäger K, Freyer D, Laube G, Bührer C, Felderhoff-Müser U, Stadelmann C, Nizet V and Weber J R 2011 *Journal of Infectious Diseases* **203** 393–400

[7] Seveau S 2014 *Sub-cellular biochemistry* **80** 161

[8] Cassidy S K B and O'Riordan M X D 2013 *Toxins* **5** 618

[9] Hamon M A, Batsché E, Régnault B, Tham T N, Seveau S, Muchardt C and Cossart P 2007 *Proceedings of the National Academy of Sciences* **104** 13467–13472

[10] Gekara N O, Jacobs T, Chakraborty T and Weiss S 2005 *Cellular Microbiology* **7** 1345–1356

[11] Martin J R, Raibaud A and Ollo R 1994 *Nature* **367** 741–745

[12] Tweten R K, Hotze E M and Wade K R 2015 *Annual Review of Microbiology* **69** 323–340

[13] Anderluh G, Kisovec M, Kraševec N and Gilbert R J C 2014 *Distribution of MACPF/CDC Proteins* (Dordrecht: Springer Netherlands) pp 7–30 ISBN 978-94-017-8881-6

[14] Dunstone M A and Tweten R K 2012 *Current opinion in structural biology* **22** 342

[15] Hadders M A, Bubeck D, Roversi P, Hakobyan S, Forneris F, Morgan B P, Pangburn M K, Llorca O, Lea S M and Gros P 2012 *Cell reports* **1** 200

[16] Reboul C F, Whisstock J C and Dunstone M A 2016 *Biochimica et Biophysica Acta (BBA) - Biomembranes* **1858** 475–486

[17] Rosado C J, Buckle A M, Law R H P, Butcher R E, Kan W T, Bird C H, Ung K, Browne K A, Baran K, Bashtannyk-Puhalovich T A, Faux N G, Wong W, Porter C J, Pike R N, Ellisdon A M, Pearce M C, Bottomley S P, Emsley J, Smith A I, Rossjohn J, Hartland E L, Voskoboinik I, Trapani J A, Bird P I, Dunstone M A and Whisstock J C 2007 *Science* **317** 1548–1551

[18] Sonnen A F, Plitzko J M and Gilbert R J 2014 *Open Biology* **4**

[19] Ruan Y, Rezelj S, Bedina Zavec A, Anderluh G and Scheuring S 2016 *PLoS Pathogens* **12** 1–18

[20] Leung C, Dudkina N V, Lukoyanova N, Hodel A W, Farabella I, Pandurangan A P, Jahan N, Pires Damaso M, Osmanović D, Reboul C F, Dunstone M A, Andrew P W, Lonnen R, Topf M, Saibil H R and Hoogenboom B W 2014 *Elife* **3** 04247

[21] Gilbert R J and Sonnen A F 2016 *European Biophysics Journal* **45** 365–376

[22] Rossjohn J, Feil S C, McKinstry W J, Tweten R K and Parker M W 1997 *Cell* **89** 685–692

[23] Shepard L A, Heuck A P, Hamman B D, Rossjohn J, Parker M W, Ryan K R, Johnson A E and Tweten R K 1998 *Biochemistry* **37** 14563–14574

[24] Shatursky O, Heuck A P, Shepard L A, Rossjohn J, Parker M W, Johnson A E and Tweten R K 1999 *Cell* **99** 293–299

[25] Heuck A P, Hotze E M, Tweten R K and Johnson A E 2000 *Molecular Cell* **6** 1233–1242

[26] Tilley S J, Orlova E V, Gilbert R J C, Andrew P W and Saibil H R 2005 *Cell* **121** 247–256

[27] Ni T, Jiao F, Yu X, Aden S, Ginger L, Williams S I, Bai F, Pražák V, Karia D, Stansfeld P, Zhang P, Munson G, Anderluh G, Scheuring S and Gilbert R J 2020 *Science Advances* **6** 1–13

[28] van Pee K, Neuhaus A, D'Imprima E, Mills D J, Kühlbrandt W and Yildiz Ö 2017 *eLife* **6** 1–22

[29] Hodel A W, Leung C, Dudkina N V, Saibil H R and Hoogenboom B W 2016 *Current Opinion in Structural Biology* **39** 8–15

[30] Leung C, Hodel A W, Brennan A J, Lukoyanova N, Tran S, House C M, Kondos S C, Whisstock J C, Dunstone M A, Trapani J A, Voskoboinik I, Saibil H R and Hoogenboom B W 2017 *Nature Nanotechnology* **12** 467

[31] Parsons E S, Stanley G J, Pyne A L B, Hodel A W, Nievergelt A P, Menny A, Yon A R, Rowley A, Richter R P, Fantner G E, Bubeck D and Hoogenboom B W 2019 *Nat Commun* **10** 2066

[32] Podobnik M, Marchioretto M, Zanetti M, Bavdek A, Kisovec M, Cajnko M M, Lunelli L, Serra M D and Anderluh G 2015 *Scientific Reports* **5** 9623

[33] Bayley H, Cronin B, Heron A, Holden M a, Hwang W L, Syeda R, Thompson J and Wallace M 2008 *Molecular bioSystems* **4** 1191–1208

[34] Leptihn S, Castell O K, Cronin B, Lee E H, Gross L C M, Marshall D P, Thompson J R, Holden M and Wallace M I 2013 *Nature Protocols* **8** 1048–1057

[35] Heron A J, Thompson J R, Cronin B, Bayley H and Wallace M I 2009 *Journal of the American Chemical Society* **131** 1652–1653

[36] Johnson B B, Moe P C, Wang D, Rossi K, Trigatti B L and Heuck A P 2012 *Biochemistry* **51** 3373–3382

[37] Thompson J R, Cronin B, Bayley H and Wallace M I 2011 *Biophysical Journal* **101** 2679

[38] Tinevez J Y, Perry N, Schindelin J, Hoopes G M, Reynolds G D, Laplantine E, Bednarek S Y, Shorte S L and Eliceiri K W 2017 *Methods* **115** 80–90

[39] Schindelin J, Arganda-Carreras I, Frise E, Kaynig V, Longair M, Pietzsch T, Preibisch S, Rueden C, Saalfeld S, Schmid B, Tinevez J Y, White D J, Hartenstein V, Eliceiri K, Tomancak P and Cardona A 2012 *Nature methods* **9**

[40] Shepard L A, Shatursky O, Johnson A E and Tweten R K 2000 *Biochemistry* **39** 10284–10293

[41] Korchev Y E, Bashford C L, Pederzolli C, Pasternak C A, Morgan P J, Andrew P W and Mitchell T J 1998 *Biochemical Journal* **329** 571–577

[42] Praper T, Sonnen A, Viero G, Kladnik A, Froelich C J, Anderluh G, Dalla Serra M and Gilbert R J 2011 *Journal of Biological Chemistry* **286** 2946–2955

[43] Kisovec M, Rezelj S, Knap P, Cajnko M M, Caserman S, Flašker A, Žnidaršič N, Repĭ M, Mavri J, Ruan Y, Scheuring S, Podobnik M and Anderluh G 2017 *Scientific Reports* **7** 1–13

[44] Keizer J 1987 *Chemical Reviews* **87** 167–180

[45] Hotze E M, Wilson-Kubalek E, Farrand A J, Bentsen L, Parker M W, Johnson A E and Tweten R K 2012 *The Journal of Biological Chemistry* **287** 24534

[46] Canny J 1986 *IEEE Transactions on Pattern Analysis and Machine Intelligence* **PAMI-8** 679–698

[47] Saffman P and Delbrück M 1975 *PNAS; Proceedings of the National Academy of Sciences* **72** 3111–3113

[48] Huang S, Romero-Ruiz M, Castell O K, Bayley H and Wallace M I 2015 *Nat Nanotechnol* **10** 986–991

[49] Palmer M, Valeva A, Kehoe M and Bhakdi S 1995 *Eur J Biochem* **231** 388–395

[50] Ramachandran R, Tweten R K and Johnson A E 2004 *Nat Struct Mol Biol* **11** 697–705

[51] Shah N R, Voisin T B, Parsons E S, Boyd C M, Hoogenboom B W and Bubeck D 2020 *Nature Communications* **11** 2–11 URL `http://dx.doi.org/10.1038/s41467-020-19482-6`

[52] Cajnko M M, Mikelj M, Turk T, Podobnik M and Anderluh G 2014 *Membrane Interactions and Cellular Effects of MACPF/CDC Proteins* (Dordrecht: Springer Netherlands) pp 119–144 ISBN 978-94-017-8881-6

[53] Nelson L D, Johnson A E and London E 2008 *Journal of Biological Chemistry* **283** 4632–4642

[54] Bhakdi S, Tranum-Jensen J and Sziegoleit A 1985 *Infection and Immunity* **47** 52–60

[55] Gilbert R J C 2002 *Cellular and Molecular Life Sciences CMLS* **59** 832–844

[56] Gilbert R J 2005 *Structure* **13** 1097–1106

[57] Flanagan J J, Tweten R K, Johnson A E and Heuck A P 2009 *Biochemistry* **48** 3977–3987

[58] Ramachandran R, Tweten R and Johnson A 2005 *PNAS; Proceedings of the National Academy of Sciences* **102** 7139–7144
[59] Smith R J M and Green C 1974 *FEBS Letters* **42** 108–111
[60] Das S K, Darshi M, Cheley S, Wallace M I and Bayley H 2007 *ChemBioChem* **8** 994–999
[61] Ulbrich M H and Isacoff E Y 2007 *Nature Methods* **4** 319–321
[62] Chung S H and Kennedy R A 1991 *Journal of Neuroscience Methods* **40** 71–86

7. Supplementary Information

7.1. Movie S1: PFO assembly

Movie of PFO assembly on a DIB by single-molecule Total Internal Reflection Fluorescence microscopy. Video starts 70 s after injection of PFO in the droplet and continues for 90 s, corresponding to the data in 1b. Images are false-coloured. Exposure time 60 ms per frame and the laser power incident at the back aperture of the objective lens was 0.25 mW.

7.2. Movie S2: PFO plasticity

Example PFO plasticity event during assembly corresponding to the data in 4. Again PFO assembly was tracked a DIB by single-molecule Total Internal Reflection Fluorescence microscopy. Exposure time 60 ms per frame and the laser power incident at the back aperture of the objective lens was 0.25 mW.

7.3. Figure S1: Stepfinding Algorithm

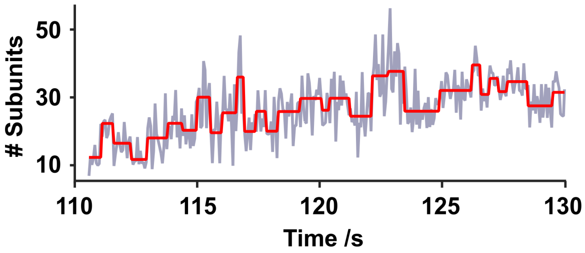

Figure 6: **Stepwise fluctuations in intensity within a nascent complex.** A step-finding algorithm ([46]) applied to a stoichiometry trajectory from 2c (highlighted as a shaded red box) shows step-wise changes in intensity.

7.4. Figure S2: Intensity calibration of PFO-a488 stoichiometry

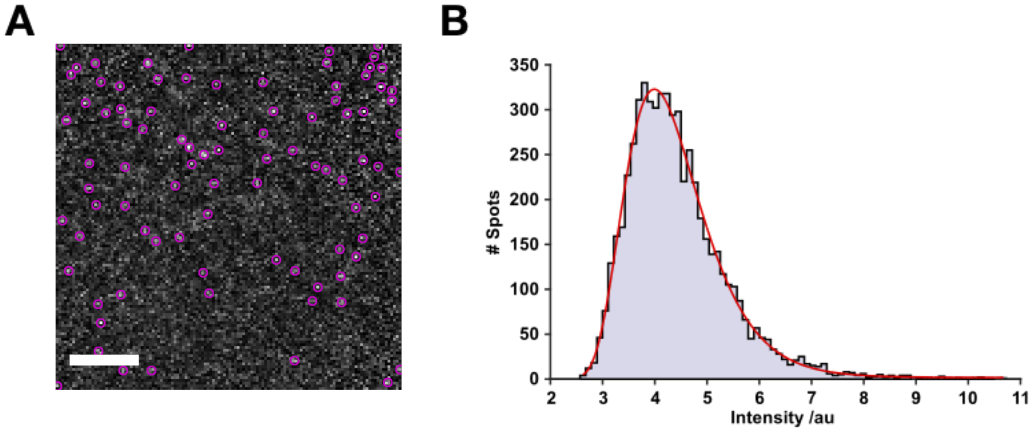

Figure 7: **Estimating single-fluorophore intensity by tracking single labelled monomers.** (A) PFO-a488 bound to a DIB membrane at a concentration (100 pM) insufficient to initiate assembly. Diffusing monomers were tracked as indicated by the purple circles. Scale bar 10 µm. (B) Following normalisation to the distribution of incident laser intensity, a histogram of pixel intensities from the detected monomer spots in a 50-frame window was plotted. The histogram was fitted with a log-normal function and the modal intensity used to calibrate stoichiometry during assembly. The intensity of each assembled complex is multiplied by the labelling ratio and divided by the single-fluorophore intensity, to estimate the number of monomers within an individual complex.

7.5. Figure S3: Photobleaching calibration of PFO-a488 stoichiometry

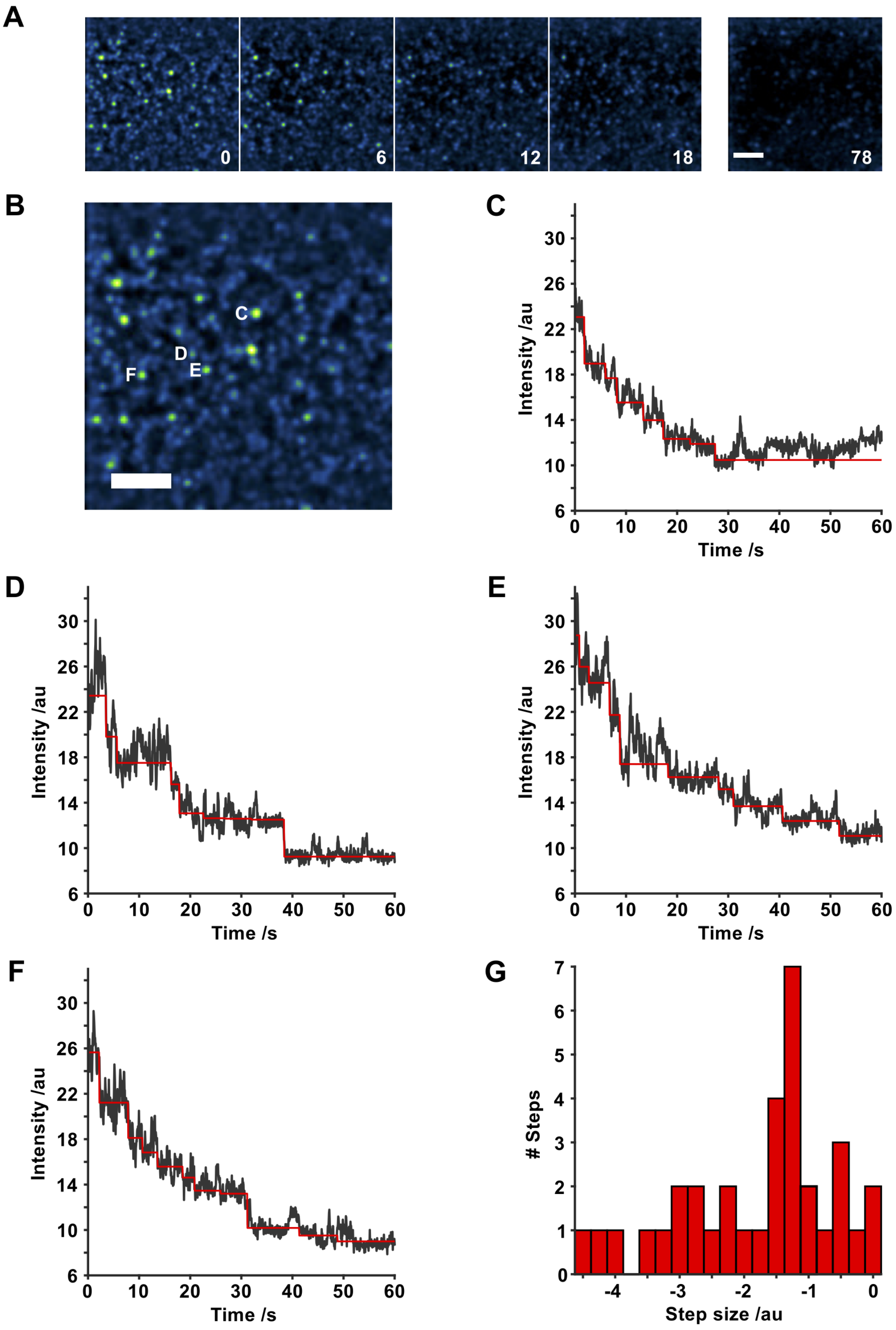

Figure 8: **Estimating single-fluorophore intensity photobleaching.** Subunit counting by photobleaching ([60, 61]) was undertaken with PFO-a488. PFO complexes were assembled in the dark, before illumination and imaging to photobleach individual complexes (0.9 mW at the objective back aperture). Plotting the intensity of complexes over time and then applying a Chung-Kennedy step-finding algorithm ([62]) to the traces highlighted the stepwise decrements due to photobleaching. (A) Montage illustrating photobleaching PFO-a488 on a DIB. Numbering indicates seconds following illumination. Scale bar 10 µm. (B) Enlarged image of the 0 s frame in A highlighting the spots show in C-F. (C-F) Representative mean intensities for example spots shown in B. Red line is the result of Cheung-Kennedy step-finding filter. (G) A histogram of the step-sizes from C-F, median step-size = -1.4 a.u. After background correction and accounting for the ratio of labelled to unlabelled PFO the number of monomers per complex in this image was estimated at 32-65, in agreement with our intensity-based calibration.

7.6. *Figure S4: Optical single channel recording from PFO*

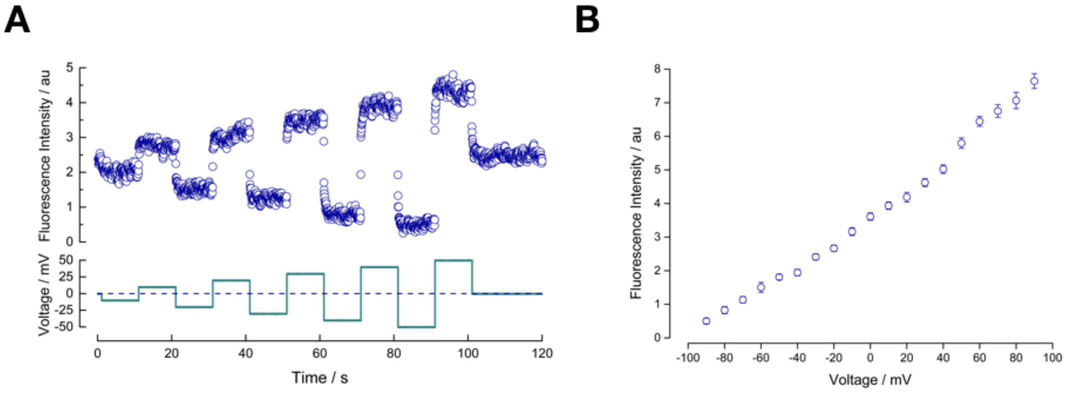

Figure 9: **Voltage response of optical single-channel recording from PFO.** (A) Time dependent responses to applied steps in membrane potential from a single PFO pore present in a DIB, corresponding to 5a. (B) Fluorescence-voltage response of a PFO pore. Error bars represent the standard deviation from the mean fluorescence intensity.